



Hierarchical assembly of smectic liquid crystal defects at undulated interfaces

Journal:	<i>Soft Matter</i>
Manuscript ID	SM-ART-06-2020-001112.R1
Article Type:	Paper
Date Submitted by the Author:	20-Jul-2020
Complete List of Authors:	Preusse, Ryan; University of Massachusetts Boston, Department of Physics George, Elizabeth ; University of Massachusetts Boston, Department of Physics Aghvami, S.; Brandeis University, Physics Otchy, Timothy; boston university, Department of biology Gharbi, Mohamed Amine; University of Massachusetts Boston, Department of Physics

Journal Name

ARTICLE TYPE

Cite this: DOI: 00.0000/xxxxxxxxxx

Hierarchical assembly of smectic liquid crystal defects at undulated interfaces

Ryan S. Preusse,^a Elizabeth R. George,^a S. Ali Aghvami,^b Timothy M. Otchy,^c and Mohamed Amine Gharbi^{*a}

Received Date

Accepted Date

DOI: 00.0000/xxxxxxxxxx

The assembly of topological defects in liquid crystals has drawn significant interest in the last decade due to their ability to trap colloidal objects and direct their arrangements. They have also brought about a high impact in modern technologies, in particular in optics, e.g., microlens arrays, soft lithography templates, and optically selective masks. Here we study the formation of defects in smectic A liquid crystal with hybrid texture at undulated surfaces. We investigate the role of surface topography on the organization of focal conic domains (FCDs) in smectic films. We demonstrate new methods for assembling FCDs and disclinations into hierarchical structures. When the liquid crystal is heated to the nematic phase, we observe stable defect lines forming at specific locations. These defects are created to satisfy anchoring conditions and the geometry of confinement imposed by the boundaries. Once the liquid crystal is cooled to the smectic A phase, the disclinations maintain their positions, but periodic structures of reversible FCDs facing opposite directions arise between them. We report the correlation between the size of these FCDs and their eccentricities with the morphology of the interface. This work paves the way for creating new procedures to control the assembly of functional nanomaterials into tunable assemblies that may find relevance in the field of energy technology including in optoelectronic and photonic applications.

1 Introduction

The technique of self-assembly is an essential tool for the creation of novel materials in the field of soft matter^{1,2}. Many examples of self-assembly exist both in nature and technological applications³. Given its fundamental importance and its utility in industry, there is an increasing interest in developing a better understanding of the parameters that control self-assembly⁴⁻⁷. Recently, liquid crystals (LCs) have been of interest because of their potential to direct the assembly of their topological defects and colloidal particles into different patterns⁸⁻¹⁵. These structures are significant to the advancement of many industries¹⁶⁻¹⁸. In most materials, scientists and engineers strive to develop methods that prevent the formation of defects because they usually inhibit the performance of devices. However, it has been shown that the creation of defects in LCs and the control of their spa-

tial arrangement is of great interest. The properties of defects can be exploited and utilized in different applications, including within the field of optics^{19,20} and the study of directed assembly of colloids and nanoparticles²¹⁻²⁴.

An important mesophase of thermotropic liquid crystals is the Smectic-A (SmA). This class of matter is characterized by the arrangement of their rod-like molecules in parallel layers, while their long axis is perpendicular to the planes of the layers. Under particular anchoring conditions, the hybrid texture, defects known as focal conic domains (FCDs) form in the SmA. These defects consist of molecular layers “wrapping” around two curves, an ellipse and a hyperbola, which contain all singular points. The eccentricity and the size of FCDs depend strongly on the thickness of the SmA and the curvature of the film at the boundaries^{25,26}.

The ability to control the assembly of FCDs into reconfigurable structures paves the way to create new devices with tunable properties²⁷⁻²⁹. When the SmA film with hybrid texture is uniform, FCDs form arrays with hexagonal symmetry. The spatial arrangement of these defects can be controlled via the thickness of the film, the anchoring conditions, the temperature of the system, or the application of an external field. It has been shown that these regular hexagonal patterns can be used to create many appli-

^a Department of Physics, University of Massachusetts Boston, Boston, MA 02125, United States of America. Fax: +1 617 287 6050; Tel: +1 617 287 5997; E-mail: mohamed.gharbi@umb.edu

^b Department of Biology and Neurophotonics Center, Boston University, Boston, MA 02215, United States of America.

^c Department of Physics, Brandeis University, Waltham, MA 02453, United States of America.

cations, including particle manipulation systems^{30,31}, templates for lithography³², photonic and lasing applications³³, and vortex beam generators³⁴. Different techniques are employed to control the size and the arrangement of FCDs that include the confinement within a 1D channels³⁵ or micropost arrays³⁶, the use of curvature^{25,26}, the use of microwrinkle grooves³⁷, the control of anchoring using different surface chemistries³⁸ and treatments^{39,40}, or the creation of defects that arise from another phase upon crossing a phase transition^{41,42}. However, little is known about how the control of the phase transition combined with the control of the interface morphology can lead to exciting assemblies of FCDs.

In this work, we explore the effect of surface morphology on the assembly of FCDs in SmA films with hybrid texture. We confine a thermotropic liquid crystal at an undulated surface and study its texture in the nematic phase, at the nematic-SmA phase transition, and in the SmA phase. The goal of our study is to understand the relation between FCDs arrangement and the interface morphology. In particular, we are interested in studying the effect of surface curvature on the eccentricity of FCDs. Our study confirms that eccentricity is correlated with the slope of the interface. In the nematic phase, we show the formation of stable disclinations, which remain once the system is cooled to the SmA. These defects are located at precise locations in the film and separate periodic regions of FCDs facing opposite directions. We demonstrate that the shape and position of these defects are dictated by the interface topography.

2 Experimental section

We obtained our studied system by mixing 85% by weight of 4'-Octyl-4-cyanobiphenyl (8CB, purchased from Kingston Chemicals Limited that displays a SmA phase between 23 and 33°C) and 15% by weight of 4-Pentyl-4-cyanobiphenyl (5CB, purchased from Kingston Chemicals Limited that displays a nematic phase between 18 and 35°C). The 8CB/5CB mixture presents a nematic phase at room temperature and a smectic phase below $\sim 10^\circ\text{C}$. Having a nematic phase at room temperature rather than a smectic helps the preparation of the samples. By utilizing a nematic phase at room temperature, we avoid potential issues related to the high viscosity of SmA. The LC mixture is confined between a base of cross-linked polydimethylsiloxane (PDMS, from Sigma-Aldrich) and a coverslip treated with polyvinyl alcohol (PVA, purchased from Sigma-Aldrich). To achieve "hybrid" anchoring with the anchoring being homeotropic (perpendicular) in contact with the PDMS, we use PVA to impose planar anchoring on the glass substrate.

The undulated surfaces, both straight and circular, are fabricated using a resonant direct laser writing system⁴³. We start by 3D printing the designs in acrylic, then we transfer the structures into PDMS. In this study, the undulated surfaces present an amplitude around $A \approx 25 \mu\text{m}$ and a period around $\lambda \approx 300 \mu\text{m}$. We study the system under an upright optical polarizing microscope (Leica DM6 M) in transmission mode equipped with a fluorescence mode and a temperature controller (Instec TS102-mK2000A). The temperature of the LC mixture is controlled with a precision around $\sim 0.1^\circ\text{C}$. Our microscope is capable of collect-

ing and comparing the data in different modes simultaneously (bright field, polarized, and fluorescence). Also, it is equipped with an automated XYZ stage useful for 3D imaging and measurement. The images were recorded with a high-resolution digital camera (Leica DMC5400).

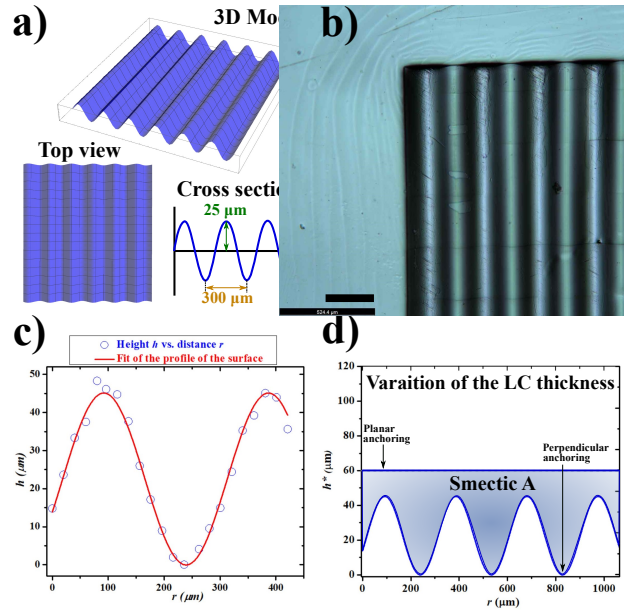


Fig. 1 Confinement of a smectic A liquid crystal at an undulated surface. (a) 3D Model showing the morphology of the interface. The amplitude of the waves is about $A \approx 25 \mu\text{m}$ and the period is about $\lambda \approx 300 \mu\text{m}$. (b) An image of an undulated structure after it is transferred to a PDMS film (scale bar: $300 \mu\text{m}$). (c) Measurement of the PDMS profile with undulations. The solid line represents the fit of profile with the expression given by equation 1. (d) A schematic showing the confinement of the LC mixture between the flat coverslip and the undulated PDMS. The thickness of the LC film h^* changes as a function of the morphology of the PDMS.

3 Results and Discussion

To measure the profile of the PDMS film, we use the microscope to scan the sample along the vertical direction while moving the stage in the horizontal direction. By detecting the top surface of the film using a high-magnification objective (x50), we measure the profile h of the PDMS film as a function of the distance r along the horizontal axis, as represented in Figure 1c. The measurements indicate the PDMS film is undulated as designed, and can be fitted to a sine wave given by the equation:

$$h(r) = h_0 + A \sin\left(\pi \frac{h - h_c}{w}\right), \quad (1)$$

where $A \approx (22.6 \pm 0.6) \mu\text{m}$ is the amplitude of the sine waves, $w = \lambda/2 \approx (147.3 \pm 1.4) \mu\text{m}$ is their half-period, $h_0 \approx (22.5 \pm 0.4) \mu\text{m}$ is the offset, and $h_c \approx (274.4 \pm 2) \mu\text{m}$ is a fitting parameter related to the phase shift of the sine function. The measure of the PDMS morphology helps to estimate the thickness of the confined LC h^* , as shown in Figure 1d. We evaluate the gap between the top flat surface of the cell and the peaks of the undulations to be around $20 \mu\text{m}$. Thus we estimate the thickness of the LC mixture h^* to vary between $20 \leq h^* \leq 60 \mu\text{m}$.

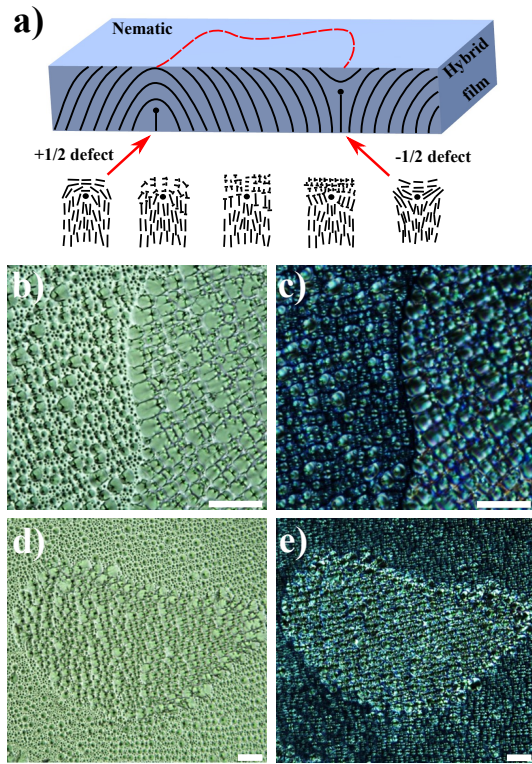


Fig. 2 Stabilization of disclinations in the SmA phase. (a) Schematic of nematic film in the presence of a disclination. The side view shows how the disclination evolves along a loop from a defect of winding number $m = -1/2$ to a defect of winding number $m = +1/2$. (b) and (c) Bright field and polarized optical microscopy images of a disclination separating two regions of FCDs facing in opposite directions. (d) and (e) Bright field and polarized optical microscopy images of a defect loop. (Scale bars: 50 μm .)

To verify the quality of anchoring conditions at the boundaries, we first analyze the texture of the smectic in the regions where the LC film is flat and uniform. When the system is in the SmA phase, we observe the formation of FCDs that assemble into ordered arrangements over large areas. These structures are reminiscent of what we obtain when a SmA is confined between a planar substrate and air. They confirm the hybrid texture of the LC mixture in our system. When the SmA is heated up to the isotropic phase then cooled down to the nematic phase, we observe distorted alignments of the director that include topological defects. These are disclinations that separate two regions of opposite orientations, as shown in Figure 2a. The nature of these disclinations evolves along a loop as described in References^{14,44}. If the system is left in the nematic phase, the loops tend to shrink and disappear after a few minutes. They vanish to minimize the excess of the elastic free energy created by defects in LCs. However, it is possible to stabilize them and control their shape using different techniques—for example, the dispersion of colloidal particles in the bulk^{45,46} or at the interface¹⁴, the confinement of the LC around micropost arrays of different geometries¹³, or by cooling the LC below the smectic-to-nematic phase transition temperature $T_{\text{SmA-N}}$ as will be shown in this study.

We first create disclinations in the nematic phase using the method of heating and cooling between the nematic and isotropic

phases. Then we stabilize the disclinations by cooling the nematic to the SmA phase before they vanish. Figures 2b and 2d show some examples of disclinations stabilized in SmA. The defects are surrounded by FCDs, facing in opposite directions. We note that the shape of the disclinations is random in the case of flat and uniform SmA films. However, our results show that controlling the morphology of the confining surface can lead to interesting assemblies of disclinations and FCDs.

When the LC is confined between the PDMS film with undulations and the planar substrate, the disclinations have different behavior in the nematic phase. They form straight lines separated by the same distance d equal to the half-period of the PDMS sine wave $d = w \approx 150 \mu\text{m}$. We investigated the properties of these disclinations using the techniques of bright field microscopy (Figure 3a) and fluorescence microscopy (Figure 3b). We found that the disclinations are stabilized by the crests and troughs of the PDMS waves. They are located at the same horizontal positions as the PDMS peaks. However, we noticed that the disclinations in the regions where LC is thick are more visible than the defects located in the thin areas. Finally, we remarked that both types of disclinations are positioned at the same vertical position, near the flat surface of the coverslip.

If the system is cooled towards $T_{\text{SmA-N}}$, we observe the formation of stripe instabilities between the disclinations. These stripes appear to reduce the bend distortion of the nematic director field, as discussed in References^{41,42}. In the nematic phase, the elastic-free energy associated with the hybrid texture can be determined using the Frank free energy:

$$F_{\text{elastic}} = \frac{1}{2} \int dV \{ K_1 (\nabla \cdot \mathbf{n})^2 + K_2 (\mathbf{n} \cdot (\nabla \times \mathbf{n}))^2 + K_3 ((\mathbf{n} \cdot \nabla) \mathbf{n})^2 - 2K_{24} \nabla \cdot [\mathbf{n}(\nabla \cdot \mathbf{n}) - (\mathbf{n} \cdot \nabla) \mathbf{n}] \}, \quad (2)$$

where K_1 , K_2 , K_3 , and K_{24} represent the elastic constants associated with the splay, twist, bend, and saddle-splay distortion modes, respectively, and \mathbf{n} is the director field of the nematic LC. In general, at the SmA-nematic phase transition, the ratio K_3/K_1 of bend to splay elastic constants diverges. However, when we approach the phase transition temperature $T_{\text{SmA-N}}$ from the nematic phase, small sinusoidal undulations of wavelength λ_{stripes} form. These are the stripe instabilities that we observe in Figures 3c and 3d. They develop to decrease the excess of the total elastic energy F_{elastic} created by the bend distortions of the nematic director. However, there is a critical value of the elastic constant K_3^* for which the instabilities form. This constant depends on both the anchoring strength W at the PDMS surface and the saddle-splay elastic constant K_{24} .

Upon cooling the nematic below the phase transition temperature $T_{\text{SmA-N}}$, we observe assemblies of FCDs between the parallel disclinations, as shown in Figures 3e and 3f and Video S1. The disclinations and the structures created by the FCDs are stable and reversible. The same assemblies occur when the SmA is heated back and forth to the isotropic phase (see Video S2 and Video S3). These results show that the fine control of anchoring conditions and the geometry of confinement could lead to the

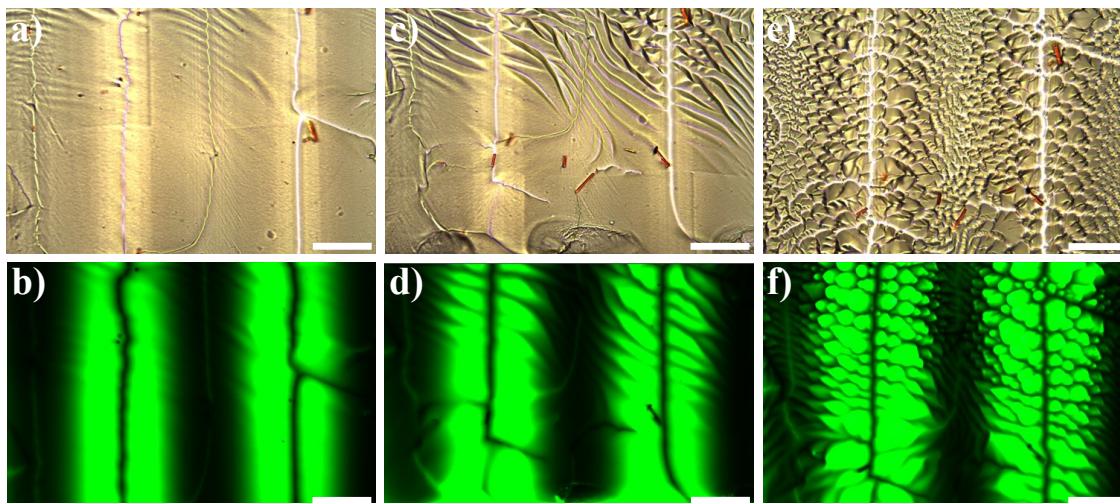


Fig. 3 FCDs formation across the nematic-SmA phase transition. (a) and (b) Bright field and fluorescence microscopy images of the disclinations forming in the nematic phase. The defect lines are found at the same horizontal position of the crests and troughs of the PDMS waves. They are separated by a distance $d \approx 150 \mu\text{m}$ equal to the half-period of the PDMS sine wave w . (c) and (d) Bright field and fluorescence microscopy images showing the formation of stripe instabilities between the disclinations near the nematic-SmA phase transition. (e) and (f) Bright field and fluorescence microscopy images showing the creation and assembly of FCDs in the SmA phase. (Scale bars: $100 \mu\text{m}$.)

stabilization of disclinations and the creation of new defect arrangements. This new process to engineer defects in nematic and SmA is robust. It paves the way for the development of a new generation of reconfigurable structures based on LCs. For example, it could be useful to create tunable assemblies of functional nanomaterials that may find relevance in the field of energy technology⁴⁷.

Figure 4 shows the assembly of FCDs in the SmA at a larger scale. These defects form periodic structures that depend on the morphology of the PDMS film. Between FCDs, we observe the presence of disclinations that are more visible in the thick region of the SmA. They can be seen in the bright field microscopy images (Figure 4a and the zoomed image in Figure 4c). However, disclinations are less defined near the thin areas of the LC film. To better investigate the presence of disclinations in thin regions, we used the technique of fluorescence microscopy. When the intensity of the excitation light is high, the disclinations become more visible (see Figure 4b and Figure 4d). These defects are similar to those near the thick regions. They separate small FCDs facing opposite directions. Our results reveal the impact of the PDMS undulations in creating disclinations in the LC. Figure 4e shows the 3D reconstruction of the periodic structure of disclinations and the hierarchical assembly of FCDs.

The thickness of the SmA film is correlated with the morphology of the PDMS film. For this reason, the size of FCDs is changing with the undulations. The same thing is noted for the eccentricity of FCDs. The elongation of the ellipses and the off-center dots marking the termination of the hyperbolæ confirm our observations. The hyperbolæ are oriented outward from the disclinations at lower peaks of the PDMS sine wave. Then, they switch orientation at the disclinations, near the top peaks. This structure is periodic, robust, and reversible.

We investigate the size distribution of FCDs as a function of the undulations to better understand the role of the PDMS morphol-

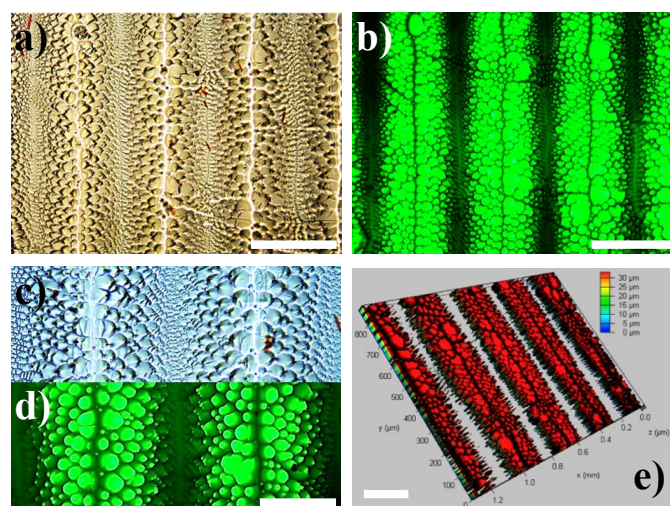


Fig. 4 Hierarchical assembly of FCDs at undulated surfaces. (a) and (b) Bright field and fluorescence microscopy images of periodic structures of FCDs arranged at undulated surfaces and separated by disclinations. The images indicate the presence of disclinations when the sign of the slope changes. (Scale bars: $300 \mu\text{m}$). (c) and (d) Bright field and fluorescence microscopy images of periodic structures of FCDs showing the non-zero eccentricity of FCDs. (Scale bar: $150 \mu\text{m}$). (e) 3D reconstruction of the hierarchical assembly of FCDs. (Scale bars: $150 \mu\text{m}$ in the horizontal direction).

ogy in the creation and the arrangement of defects in SmA. We start by measuring the area of the ellipses E occupied by FCDs (each FCD in Figures 5a is fitted to an ellipse E). We then plot these areas as a function of the distance r in the horizontal direction. We consider a disclination located near the thick region of SmA to be the origin of our analysis. The data shown in Figure 5b indicate that the areas of E are fluctuating. This is due to the presence of small FCDs packed between larger FCDs to fill the empty space, as discussed in Reference²⁶. We note here that

when the thickness of the SmA is thin, near the top peaks of the undulations, the FCDs are tiny. Unfortunately, the resolution of the image processing technique used to analyze FCDs is limited. It is unable to detect the ellipses near these regions. For this reason no data are collected there.

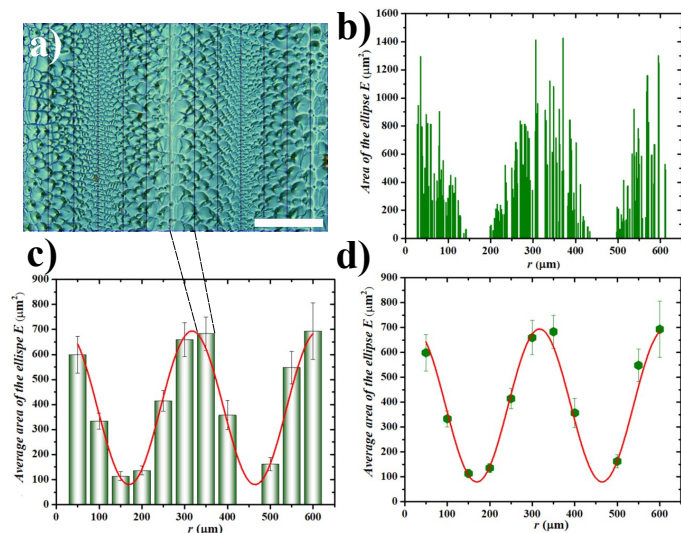


Fig. 5 Variation of FCDs along PDMS undulations. (a) An optical image of FCDs arranged at an undulated surface. The vertical lines represent the limit of the bins. These $50 \mu\text{m}$ bins are used to average the area of the ellipses E occupied by FCDs. (Scale bar: $150 \mu\text{m}$). Variation of the areas of the ellipses E as a function of the distance r , along the horizontal axis, before (b) and after we average (c). The missing data near the regions $r \approx 170 \mu\text{m}$ and $r \approx 450 \mu\text{m}$, are due to the small size of FCDs that we are unable to detect. (d) Correlation between the size of FCDs and the profile of the PDMS surface. The solid lines in (c) and (d) represent the fit of the areas with the expression given by equation 1. (Error bars are the standard deviations of the areas of E .)

To better identify the relation between the size of FCDs and the undulations, we average the areas of the ellipses E in bins of $50 \mu\text{m}$. In these regions, we assume FCDs have similar behavior. This process helps to reduce the noise induced by the presence of small defects. The results presented in Figures 5c and 5d show that FCD sizes are correlated with the profile of the confining surface, as well as the thickness of the SmA film. The size distribution is undulated. It can be fit to the same sine wave given by Equation 1, with the same half period $w_{FCDs} \approx 147.41 \pm 2 \mu\text{m}$. More generally, we illustrate how designed interfaces can provide a way to raise spatially organized FCDs. The schematic in Figure 6a reveals the difference between the arrangement of FCDs in uniform SmA films and their assembly at undulated surfaces. This model shows that FCDs of nonzero eccentricity can be organized at curved interfaces without violating the law of corresponding cones^{48–50}, as discussed in Reference²⁵. At the top and lower peaks of the PDMS wave, the sign of the interface slope changes. Then, the hyperbolæ of FCDs switch from extending inward or outward. The mismatch in orientation explains the formation of disclinations near the peaks of the undulations.

We also found that the nonzero eccentricity is correlated with the profile of the PDMS surface, as shown in Figure 6b. It decreases from a maximum at the lower peak of the undulation, and

increases when the slope's sign changes. Figure 6c shows how the eccentricity is rising reasonably with the thickness of the smectic film h^* . The FCDs nearest the thicker regions of SmA have the highest eccentricity, while those near the thin regions have the lowest eccentricity. However, the value of the eccentricity in the system is not approaching zero (between $0.45 < e < 0.7$). This could be explained by the high deformation of the smectic layer at the undulated surfaces, which imposes homeotropic anchoring while the anchoring at the horizontal substrate is degenerate planar.

We tried to investigate if the tilt grain boundary model conforms with the FCD eccentricities e in our system. In this model, if the homeotropic interface is curved, the eccentricity should increase with the slope of the interface. The relation between the eccentricity e and the slope of the homeotropic interface dh^*/dr is given by⁵⁰:

$$e = \left[\frac{(dh^*/dr)^2}{1 + (dh^*/dr)^2} \right]^{\frac{1}{2}}. \quad (3)$$

Qualitatively, this model should agree with our experimental results. We see the eccentricity increasing and decreasing with the undulations (Figure 3b). Quantitatively, however, this model disagrees with the FCD eccentricities e in our system and does not fit our data. We believe this difference is due to the high curvature of the designed undulations since the model considers the homeotropic interface to be a tilted plane.

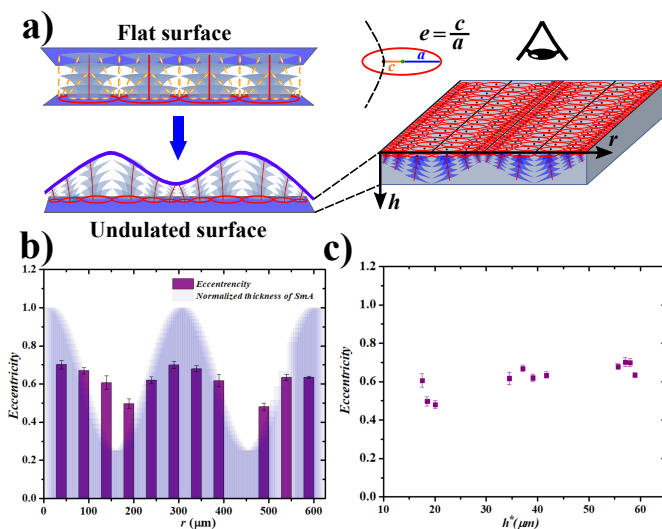


Fig. 6 Effect of the PDMS morphology on the eccentricity of FCDs. (a) 3D model describing the difference between the arrangement of FCDs at flat and at undulated surfaces. (b) Variation of the FCD eccentricity as a function of the distance r . The undulations represent the normalized thickness of the SmA. (c) Variation of the eccentricity as a function of the SmA thickness h^* . (Error bars are the standard deviations of the eccentricity.)

We previously demonstrate how the morphology of the confining surface dictates the type of defects, their size, their packing, and how they assemble. To confirm the role of surface morphology, we design a new system with circular undulations (Figure 7). The amplitude of the waves and their period are identical to

those of the vertical undulations. We observe the formation of disclinations at the peaks of the waves. These defect lines have circular structures to mimic the shape of the PDMS surface. They separate FCDs that form in packings similar to those described in the first system. This new hierarchical assembly of FCDs with different eccentricity at this novel geometry proves the effect of the boundaries; geometry and anchoring combined.

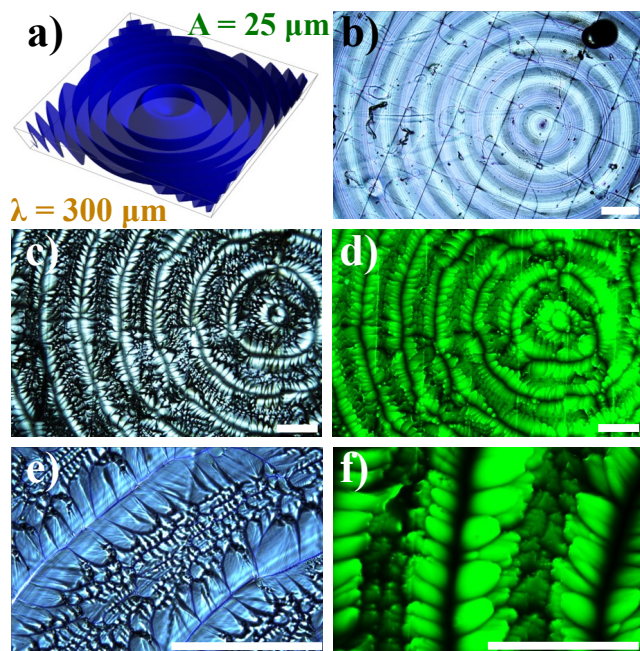


Fig. 7 Assembly of disclinations and FCDs at circular waves. (a) 3D Model showing the morphology of the interface. The amplitude and period of the waves are the same as those of the first system ($A \approx 25 \mu\text{m}$ and $\lambda \approx 300 \mu\text{m}$). (b) Bright field image of the LC mixture confined at the circular waves in the isotropic phase. (c) and (d) Bright field and fluorescence microscopy images of periodic structures of FCDs arranged at undulated surfaces of a different geometry and separated by circular disclinations. (e) and (f) Bright field and fluorescence microscopy images of disclinations and FCDs at a higher magnification. (Scale bars: $300 \mu\text{m}$.)

Our results show that by changing the design of the confining surface and by preserving careful control of the anchoring conditions at the boundaries, we can guide the assembly of FCDs and their associated disclinations into reconfigurable structures. This study reveals that the procedure used here is robust. It will open the door to crafting novel self-assembled patterns. The development of this approach will play an essential role in modern technological applications based on the assembly of functional nanomaterials and biomaterials. The most important key feature here is the clever preparation of the boundaries.

4 Conclusion

We report a novel procedure to direct the assembly of defects in SmA LC. We detail the role of the geometry at the boundaries in creating hierarchical structures of FCDs. Near the nematic-SmA phase transition, we develop disclinations of random shapes. These disclinations are stabilized in the SmA using an undulated surface of PDMS. However, to satisfy the hybrid anchoring condi-

tion imposed by the boundaries, the SmA creates FCDs arranged in periodic structure between the disclinations. The size of these defects and their eccentricity are correlated with the morphology of the confining surface. By changing the geometry of the boundaries, we can design new means to assemble disclinations and FCDs. This work paves the way to explore new means to fabricate novel devices with reconfigurable properties. Moreover, it suggests new strategies to make hierarchical functional structures, as FCDs and disclinations have been used to organize nanoparticles within their cores.

Author Contributions

R.S.P., E.R.G., and M.A.G. performed the research; M.A.G. designed the experiments; R.S.P., S.A.A., T.M.O. and M.A.G. designed the 3D printed structures; R.S.P. and E.R.G. analyzed the data; R.S.P., and M.A.G. wrote the manuscript. All authors have reviewed the manuscript.

Conflicts of interest

There are no conflicts to declare.

Acknowledgements

This research was funded by the University of Massachusetts Boston. E.R.G was supported by UMass Boston College of Science and Mathematics Dean's Research Fellowship from Oracle. The authors acknowledge Brandeis MRSEC (NSF-MRSEC-2011486) for use of the Clean Room Facility.

Notes and references

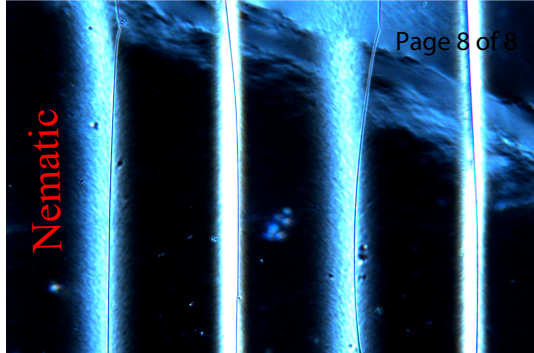
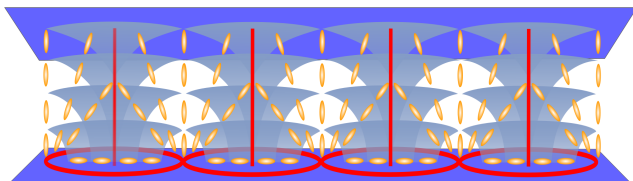
- 1 E. M. Furst, *Soft Matter*, 2013, **9**, 9039–9045.
- 2 M. Grzelczak, J. Vermant, E. M. Furst and L. M. Liz-Marzán, *ACS Nano*, 2010, **4**, 3591–3605.
- 3 A. D. Rey, *Soft Matter*, 2010, **6**, 3402–3429.
- 4 C. K. Ober, *Nature Nanotechnology*, 2017, **12**, 507–508.
- 5 J. Xu, Z. Wang, F. Zhang, S. Peng, J. Zhang and L. Zhang, *Macromolecular Rapid Communications*, 2020, **41**, 1900505.
- 6 B. Oruc, S. Celik, S. H. Soytaş and H. Unal, *ACS Omega*, 2018, **3**, 4157–4162.
- 7 J. A. Martínez-González, X. Li, M. Sadati, Y. Zhou, R. Zhang, P. F. Nealey and J. J. D. Pablo, *Nature Communications*, 2017, **8**, 1–9.
- 8 C. Blanc, D. Coursault and E. Lacaze, *Liquid Crystals Reviews*, 2013, **1**, 83–109.
- 9 X. Wang, D. S. Miller, E. Bukusoglu, J. J. D. Pablo and N. L. Abbott, *Nature Materials*, 2016, **15**, 106–112.
- 10 F. Serra, *Liquid Crystals*, 2016, **43**, 1920–1936.
- 11 I. Musevič and M. Skarabot, *Soft Matter*, 2008, **4**, 195.
- 12 I. I. Smalyukh, *Annual Review of Condensed Matter Physics*, 2018, **9**, 207–226.
- 13 M. Cavallaro, M. A. Gharbi, D. A. Beller, S. Copar, Z. Shi, T. Baumgart, S. Yang, R. D. Kamien and K. J. Stebe, *Proceedings of the National Academy of Sciences of the United States of America*, 2013, **110**, 18804–18808.
- 14 M. A. Gharbi, M. Nobili and C. Blanc, *Journal of Colloid and Interface Science*, 2014, **417**, 250–255.

- 15 M. J. Shin, M. J. Gim and D. K. Yoon, *Langmuir*, 2018, **34**, 2551–2556.
- 16 S. J. Woltman, G. D. Jay and G. P. Crawford, *Nature Materials*, 2007, **6**, 929–938.
- 17 J. Beeckman, *Optical Engineering*, 2011, **50**, 081202.
- 18 J. P. Lagerwall and G. Scalia, *Current Applied Physics*, 2012, **12**, 1387–1412.
- 19 F. Serra, M. A. Gharbi, Y. Luo, I. B. Liu, N. D. Bade, R. D. Kamien, S. Yang and K. J. Stebe, *Advanced Optical Materials*, 2015, **3**, 1287–1292.
- 20 Y. H. Kim, J.-O. Lee, H. S. Jeong, J. H. Kim, E. K. Yoon, D. K. Yoon, J.-B. Yoon and H.-T. Jung, *Advanced Materials*, 2010, **22**, 2416–2420.
- 21 I. Mušević, M. Škarabot, U. Tkalec, M. Ravnik and S. Žumer, *Science*, 2006, **313**, 954–958.
- 22 X. Li, J. C. Armas-Pérez, J. P. Hernández-Ortiz, C. G. Arges, X. Liu, J. A. Martínez-González, L. E. Ocola, C. Bishop, H. Xie, J. J. D. Pablo and P. F. Nealey, *ACS Nano*, 2017, **11**, 6492–6501.
- 23 S. P. Do, A. Missaoui, A. Coati, D. Coursault, H. Jeridi, A. Resta, N. Goubet, M. M. Wojcik, A. Choux, S. Royer, E. Briand, B. Donnio, J. L. Gallani, B. Pansu, E. Lhuillier, Y. Garreau, D. Babonneau, M. Goldmann, D. Constantin, B. Gallas, B. Croset and E. Lacaze, *Nano Letters*, 2020, **20**, 1598–1606.
- 24 M. Bartolo, J. J. Amaral, L. S. Hirst and S. Ghosh, *Scientific Reports*, 2019, **9**, 1–11.
- 25 D. A. Beller, M. A. Gharbi, A. Honglawan, K. J. Stebe, S. Yang and R. D. Kamien, *Physical Review X*, 2014, **3**, 041026.
- 26 M. A. Gharbi, I. B. Liu, Y. Luo, F. Serra, N. D. Bade, H. N. Kim, Y. Xia, R. D. Kamien, S. Yang and K. J. Stebe, *Langmuir*, 2015, **31**, 11135–11142.
- 27 Y. H. Kim, H. S. Jeong, J. H. Kim, E. K. Yoon, D. K. Yoon and H. T. Jung, *Journal of Materials Chemistry*, 2010, **20**, 6557–6561.
- 28 D. S. Kim and D. K. Yoon, *Journal of Information Display*, 2018, **19**, 7–23.
- 29 Y. Xia, A. Honglawan and S. Yang, *Liquid Crystals Reviews*, 2019, **7**, 30–59.
- 30 A. Honglawan, D. S. Kim, D. A. Beller, D. K. Yoon, M. A. Gharbi, K. J. Stebe, R. D. Kamien and S. Yang, *Soft Matter*, 2015, **11**, 7367–7375.
- 31 M. A. Gharbi, D. A. Beller, N. Sharifi-Mood, R. Gupta, R. D. Kamien, S. Yang and K. J. Stebe, *Langmuir*, 2018, **34**, 2006–2013.
- 32 D. K. Yoon, M. C. Choi, Y. H. Kim, M. W. Kim, O. D. Lavrentovich and H. T. Jung, *Nature Materials*, 2007, **6**, 866–870.
- 33 K. Peddireddy, V. S. R. Jampani, S. Thutupalli, S. Herminghaus, C. Bahr and I. Mušević, *Optics Express*, 2013, **21**, 30233.
- 34 B. Son, S. Kim, Y. H. Kim, K. Kälántár, H.-M. Kim, H.-S. Jeong, S. Q. Choi, J. Shin, H.-T. Jung and Y.-H. Lee, *Optics Express*, 2014, **22**, 4699.
- 35 C. C. Myung, T. Pfohl, W. Zhiyu, L. Youli, W. K. Mahn, J. N. Israelachvili and C. R. Safinya, *Proceedings of the National Academy of Sciences of the United States of America*, 2004, **101**, 17340–17344.
- 36 A. Honglawan, D. A. Beller, M. Cavallaro, R. D. Kamien, K. J. Stebe and S. Yang, *Advanced Materials*, 2011, **23**, 5519–5523.
- 37 T. Ohzono, Y. Takenaka and J. I. Fukuda, *Soft Matter*, 2012, **8**, 6438–6444.
- 38 P. Prompinit, A. S. Achalkumar, J. P. Bramble, R. J. Bushby, C. Wälti and S. D. Evans, *ACS Applied Materials and Interfaces*, 2010, **2**, 3686–3692.
- 39 S. H. Ryu, M. J. Gim, Y. J. Cha, T. J. Shin, H. Ahn and D. K. Yoon, *Soft Matter*, 2015, **11**, 8584–8589.
- 40 W. Guo, S. Herminghaus and C. Bahr, *Langmuir*, 2008, **24**, 8174–8180.
- 41 M. J. Gim, D. A. Beller and D. K. Yoon, *Nature Communications*, 2017, **8**, 1–9.
- 42 A. Suh, M. J. Gim, D. Beller and D. K. Yoon, *Soft Matter*, 2019, **15**, 5835–5841.
- 43 B. W. Pearre, C. Michas, J. M. Tsang, T. J. Gardner and T. M. Otchy, *Additive Manufacturing*, 2019, **30**, 100887.
- 44 M. Kléman and O. Lavrentovich, *Soft Matter Physics: An Introduction Springer (2003)*, Springer, 2003.
- 45 D. Pires, J. B. Fleury and Y. Galerne, *Physical Review Letters*, 2007, **98**, 247801.
- 46 M. Škarabot, M. Ravnik, S. Žumer, U. Tkalec, I. Poberaj, D. Babič and I. Mušević, *Physical Review E - Statistical, Non-linear, and Soft Matter Physics*, 2008, **77**, 061706.
- 47 J. M. Ok, Y. H. Kim, T. Y. Lee, H. W. Yoo, K. Kwon, W. B. Jung, S. H. Kim and H. T. Jung, *Langmuir*, 2016, **32**, 13418–13426.
- 48 J. P. Sethna and M. Kléman, *Physical Review A*, 1982, **26**, 3037–3040.
- 49 O. Lavrentovich, *Sov Phys JETP*, 1986, **91**, 1666–1676.
- 50 M. Kléman and O. D. Lavrentovich, *European Physical Journal E*, 2000, **2**, 47–57.

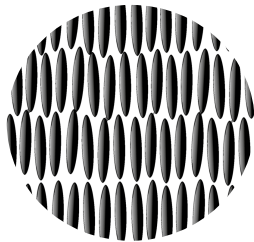
Flat Surface

Soft Matter

Page 8 of 8

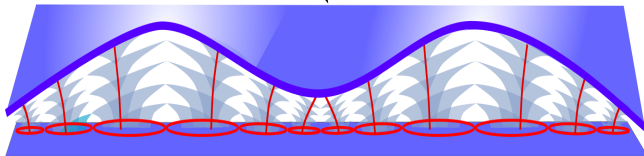


Surface Morphology



Smectic A

Assembly of disclinations and FCDs



Undulated Surface

